



# Transient supercritical droplet evaporation with emphasis on the effects of equation of state

G.S. Zhu<sup>1</sup>, S.K. Aggarwal\*

*Department of Mechanical Engineering (M/C 251), University of Illinois at Chicago, 842 W. Taylor Street, RM 2039, Chicago, IL 60607-7022, USA*

Received 25 November 1998; received in revised form 2 June 1999

## Abstract

This paper reports a numerical investigation of droplet evaporation in a supercritical environment. A comprehensive physical–numerical model is developed to simulate the transcritical and supercritical droplet vaporization phenomena. The model is based on the time-dependent conservation equations for both liquid and gas phases, pressure-dependent variable thermophysical properties, and a detailed treatment of liquid–vapor phase equilibrium at the droplet surface. The numerical solution of the two-phase equations employs an arbitrary Eulerian–Lagrangian, explicit–implicit method with a dynamically adaptive mesh. The first part of the study examines the capability of different equations of state (EOS) for predicting the phase equilibrium and transcritical droplet vaporization behavior. Predictions using the Redlich–Kwong (RK) EOS are shown to be markedly different from those using the Peng–Robinson (PR) and Soave–Redlich–Kwong (SRK) EOS. Results for the phase-equilibrium of a *n*-heptane–nitrogen system indicate that compared to PR- and SRK-EOS, the RK-EOS predicts higher fuel vapor concentration, higher liquid-phase solubility of nitrogen, lower critical-mixing-state temperature, and lower enthalpy of vaporization. As a consequence, it significantly overpredicts droplet vaporization rates and, thus, underpredicts droplet lifetimes compared to those predicted by PR- and SRK-EOS, as well as compared to experimental data. Furthermore, using RK-EOS, attainment of the critical mixing state at the droplet surface is predicted earlier in droplet lifetime compared with that using the other two EOS. In contrast, predictions using the PR-EOS show excellent agreement with experimental data over a wide range of ambient conditions. The PR-EOS is then used for a detailed investigation of the transcritical droplet vaporization phenomena. Results indicate that at low to moderate ambient temperatures, the droplet lifetime first increases and then decreases as the ambient pressure is increased, while at high ambient temperatures, the droplet lifetime decreases monotonically with pressure. This behavior is in accord with the published experimental results. The numerical model is also used to obtain the minimum pressure required for the attainment of critical mixing state at the droplet surface for a given ambient temperature. © 1999 Elsevier Science Ltd. All rights reserved.

## 1. Introduction

Droplet gasification in a supercritical environment is a phenomena of immense practical interest. In diesel and liquid rocket engines, spray atomization/vaporization occur in transcritical and/or supercritical conditions. In jet engines used in military applications, the

\* Corresponding author. Tel.: +1-312-996-2235; fax: +1-312-413-0447.

*E-mail address:* ska@uic.edu (S.K. Aggarwal)

<sup>1</sup> Visiting Scholar from Nanjing University of Science and Technology, China.

liquid fuel is the primary coolant for on-board heat sources, and may attain a critical state before it is 'atomized'. The gas turbine combustors used in propulsion applications are also being designed to operate at pressures, which may exceed the critical pressure of the fuel. The fundamental processes associated with transcritical phase-change and supercritical transport are also relevant to other applications including chemical processing and environmental control using supercritical fluids.

The modeling of transcritical droplet gasification also represents a scientifically challenging problem, since the conventional 'low-pressure' droplet models are generally not valid at high-pressure conditions. For example, the gas-phase non-idealities and the liquid-phase solubility of gases are negligible at low pressures, but become essential considerations at high pressures. Consequently, a single-component fuel droplet would assume a multicomponent behavior, and liquid mass transport in the droplet interior would become an important process. Secondly, as the droplet surface approaches the transcritical state, the latent heat reduces to zero, and the gas and liquid densities become equal at the droplet surface. Then, transient effects in the gas phase would become as important as those in the liquid phase, since the characteristic times for transport processes in the two phases become comparable. In addition, the liquid- and gas-phase thermophysical properties become pressure-dependent. Also, under convective conditions, the droplet distortion and breakup become important processes, as the surface tension is greatly diminished and approaches zero at the critical point.

Due to its significant practical and fundamental relevance, the supercritical droplet gasification phenomena has been a subject of many theoretical and experimental investigations. Manrique and Borman [1] presented a methodology to consider several high-pressure effects in a quasi-steady model. In their model, the Redlich–Kwong equation of state (RK-EOS) [2] was employed to describe the real gas behavior. However, the gas-phase processes were assumed to be in quasi-steady state, and the liquid phase heating in the droplet interior was neglected. In a subsequent study [3], it was demonstrated that effects due to thermodynamic non-idealities and property variations modified the vaporization behavior significantly. Lazar and Faeth [4] and Canada and Faeth [5] also employed RK-EOS to develop a high-pressure model to investigate steady-state droplet vaporization and combustion for hydrocarbon fuels. They found the droplet burning-rate predictions of the high-pressure model to be similar to those of a conventional low-pressure model. In addition, the results of both models were in fair agreement with their experimental data. Matlosz et al. [6] also developed a high-pressure model

in which the gas-phase unsteadiness and real gas effects were included, while the gas absorption in liquid droplet was neglected. They found that the gas-phase non-idealities were important for the prediction of droplet temperature and size histories.

Curtis and Farrell [7,8] developed a high-pressure model using the Peng–Robinson equation of state (PR-EOS) [9] that predicted the droplet vaporization rate and temperature as well as the critical mixing state. In addition, it was shown that for droplet vaporization under conditions similar to those in diesel engines, the anomalies in transport properties near the critical mixing state were insignificant. Hsieh et al. [10] reported a comprehensive analysis of the high-pressure droplet vaporization phenomena in binary and ternary systems at a temperature of 2000 K. The Soave–Redlich–Kwong equation of state (SRK-EOS) [11] was employed in the analysis. In a subsequent study, Shuen et al. [12] extended this high-pressure model to examine the combustion behavior of a *n*-pentane droplet under subcritical and supercritical conditions. Their results indicated a continuous increase in the droplet gasification rate with pressure, with a more rapid increment occurring near the critical burning pressure of the fuel. Delpanque and Sirignano [13] also considered a transient, spherically-symmetric model to investigate transient gasification of a liquid oxygen droplet in gaseous hydrogen at high pressures. It was noted that at supercritical pressures, the droplet surface temperature reaches the critical mixing value. Jia and Gogos [14,15] employed the PR-EOS to quantify the effect of liquid-phase gas solubility on the vaporization of a *n*-hexane droplet for a range of ambient pressures and temperatures. It was shown that the liquid-phase gas solubility becomes increasingly important as the ambient pressure approaches the critical value. In addition, the variation of droplet lifetime with pressure was shown to exhibit a maximum at low ambient temperatures, but to decrease monotonically with pressure at high ambient temperatures. Stengel et al. [16] employed the SRK-EOS to examine the vaporization behavior of freely falling *n*-heptane droplets in a nitrogen environment. Results from a quasi-steady droplet model were compared with measurements for ambient pressure up to 40 atm. Aggarwal et al. [17] also reported a quasi-steady high-pressure model that used the PR-EOS and included the transient liquid-phase processes, as well as the effect of pressure on thermophysical properties. The predicted vaporization histories were shown to compare well with the measurements of Stengel et al. [16].

Ruszalo and Hallett [18] employed the PR-EOS to examine the droplet ignition phenomena at high pressures. Their analysis considered a simplified liquid-phase model by assuming a uniform liquid temperature inside the droplet. In addition, the transport properties

were assumed to be temporally varying but spatially uniform. Numerical results indicated that the ignition delay time decreases substantially at high pressures. However, the liquid-phase gas solubility was found to have a negligible influence on the ignition delay time, and no fundamental or abrupt change in ignition phenomena was observed as the ambient pressure exceeded the critical value.

An important result emerging from previous numerical and experimental investigations [19–22] is that a droplet does not immediately attain the critical mixing state as it is introduced into an ambient where the pressure and temperature exceed the thermodynamic critical point of the liquid fuel. Also, while most studies indicate that the droplet surface generally reaches the critical mixing state at some pressure that is much higher than the fuel critical pressure, they report a wide scatter in the minimum ambient pressure required to reach the critical state. Previous investigations have not quantified the effects of other parameters, especially ambient temperature, on this minimum pressure. The literature review also indicates that several different EOS have been employed to represent the liquid–vapor phase equilibrium at the droplet surface. Clearly, an accurate representation of phase equilibrium is essential for a realistic simulation of droplet evaporation at high pressures. However, previous studies have not examined in detail the accuracy of various EOS and their effects on the supercritical droplet evaporation. The present study is motivated by these considerations. Another important consideration stems from the fact that processes characterizing the transcritical phenomena are not adequately understood at present.

In the present investigation, a comprehensive model is developed to investigate the transcritical/supercritical droplet vaporization phenomena. The model is first used to examine the effects of different EOS on the prediction of phase equilibrium for a *n*-heptane–nitrogen system, as well as on the prediction of droplet gasification rate in a supercritical environment. A detailed numerical study is then conducted to characterize the transcritical vaporization phenomena, including the transition from subcritical to supercritical state, and the subsequent supercritical droplet gasification behavior. Predictions are compared with the available experimental data.

Several recent investigations [8,10,14] have employed a transient spherically model to examine droplet vaporization under supercritical conditions. It is important, therefore, to delineate the differences between the present and these previous investigations. One notable difference is that a more complete model is employed in the present study, since (1) it considers mass, momentum, species, and energy conservation equations; many previous studies do not consider the

momentum equation and, thus, do not accurately capture the gas-phase unsteadiness, especially the viscous effects, which become important at high pressures; (2) it considers the absorption of gas in the liquid phase and resolves the mass diffusion process within the droplet; (3) it considers both the gas- and liquid-phase properties to be functions of species, temperature and pressure; and (4) it employs an adaptive grid. In addition, a comprehensive analysis of the transcritical phenomenon is performed, and a detailed investigation of the different equations of state as well as a detailed comparison with experimental data is presented.

## 2. Problem formulation

The physical problem described here considers the transient gas- and liquid-phase processes associated with an isolated fuel droplet. The droplet is initially at a sub-critical state and suddenly introduced into a stagnant gas environment with its thermodynamic state in the supercritical regime of the fuel species. The transient, two-phase governing equations are written in a spherical coordinate system. The radiation and second-order effects, such as the Soret and Dufour effects, are assumed to be negligible. The governing equations and the interphase conditions at the droplet surface are described as follows.

### 2.1. Governing equations

For the gas-phase region  $r > r_s(t)$ , the governing equations include the conservation equations for species, momentum, energy, and the equation of state (EOS):

$$\frac{\partial \rho_k}{\partial t} + \frac{1}{r^2} \frac{\partial}{\partial r} (\rho_k u r^2) = \frac{1}{r^2} \frac{\partial}{\partial r} \left[ \rho D_k r^2 \frac{\partial}{\partial r} \left( \frac{\rho_k}{\rho} \right) \right] + \rho_k^c \quad (1)$$

$$\begin{aligned} \frac{\partial \rho u}{\partial t} + \frac{1}{r^2} \frac{\partial}{\partial r} (\rho u^2 r^2) + \frac{\partial p}{\partial r} &= \frac{1}{r^2} \frac{\partial}{\partial r} \left[ 2\mu r^2 \frac{\partial u}{\partial r} + \lambda \frac{\partial}{\partial r} (u r^2) \right] \\ &- \frac{2}{r^2} \left[ 2\mu u + \frac{\lambda}{r} \frac{\partial}{\partial r} (u r^2) \right] \end{aligned} \quad (2)$$

$$\begin{aligned} \frac{\partial \rho I}{\partial t} + \frac{1}{r^2} \frac{\partial}{\partial r} (\rho I u r^2) + \frac{p}{r^2} \frac{\partial}{\partial r} (u r^2) \\ &= \frac{1}{r^2} \left\{ \frac{\partial}{\partial r} r^2 \rho D_k \left[ \sum_{k=1}^N h_k \frac{\partial}{\partial r} \left( \frac{\rho_k}{\rho} \right) \right] \right\} \\ &+ \frac{1}{r^2} \frac{\partial}{\partial r} \left( k r^2 \frac{\partial T}{\partial r} \right) + \frac{\partial u}{\partial r} \left[ 2\mu \frac{\partial u}{\partial r} + \frac{\lambda}{r^2} \frac{\partial}{\partial r} (u r^2) \right] \\ &+ \frac{2u}{r^2} \left[ 2\mu u + \frac{\lambda}{r} \frac{\partial}{\partial r} (u r^2) \right] + Q_c \end{aligned} \quad (3)$$

$$f_1(p, T, \rho_1, \rho_2, \dots, \rho_N) = 0 \tag{4}$$

In the above equations,  $t$  and  $r$  refer to temporal and spatial variables, respectively,  $r_s(t)$  is the instantaneous droplet radius, and  $D_k$ ,  $\rho_k$ , and  $h_k$  are the diffusion coefficient, density and specific enthalpy of  $k$ th species, respectively.  $N$  is the total number of species. Further,  $k$ ,  $\mu$ , and  $\lambda$  are the thermal conductivity, viscosity, and second viscosity coefficient, respectively. The last term in the right-hand side of Eqs. (1) and (3), which represents the mass or energy source term associated with chemical reactions, is taken as zero since an evaporating droplet is simulated in the present study. Eq. (4) represents a  $P$ - $V$ - $T$  relation for the fluid mixture. A cubic EOS is employed, which can be written in a general form as [23,24]:

$$p = \frac{RT}{V-b} - \frac{a}{V^2 + ubV + wb^2} \tag{5}$$

where  $a$  and  $b$  are functions of temperature and species mole fractions. In order to employ this equation for a multi-component mixture, some mixing rules are needed.  $u$  and  $w$  are constants. Their values are:  $u = 2$ ,  $w = -1$  for PR-EOS; and  $u = 1$ ,  $w = 0$  for SRK-EOS and RK-EOS.

For the liquid-phase region,  $r < r_s$ , the governing equations are the energy and species equations:

$$\frac{\partial}{\partial t} (\rho_l C_{pl} T_l) = \frac{1}{r^2} \frac{\partial}{\partial r} \left( k_l r^2 \frac{\partial T_l}{\partial r} \right) + \frac{1}{r^2} \frac{\partial}{\partial r} \left[ r^2 \sum_{k=1}^N \rho_l D_l h_k \frac{\partial}{\partial r} \left( \frac{\rho_{lk}}{\rho_l} \right) \right] \tag{6}$$

$$\frac{\partial \rho_{lk}}{\partial t} = \frac{1}{r^2} \frac{\partial}{\partial r} \left[ \rho_{lk} D_l r^2 \frac{\partial}{\partial r} \left( \frac{\rho_{lk}}{\rho_l} \right) \right] \tag{7}$$

where the subscript ‘l’ denotes the liquid phase, and  $C_p$  is the specific heat at constant pressure.

### 2.2. Boundary conditions

On the droplet surface,  $r = r_s$ , the conditions of mass and energy conservation, and of thermodynamic equilibrium are represented as:

$$\dot{m} X_k - \rho_{lk} D_l \frac{\partial X_k}{\partial r} \Big|_{r=r_s^-} = \dot{m} Y_k - \rho_k D_k \frac{\partial Y_k}{\partial r} \Big|_{r=r_s^+} \tag{8}$$

$$\begin{aligned} -k_l \frac{\partial T_l}{\partial r} \Big|_{r=r_s^-} &= -k \frac{\partial T}{\partial r} \Big|_{r=r_s^+} \\ &+ \sum_{k=1}^N \left( \dot{m} Y_k - \rho_k D_k \frac{\partial Y_k}{\partial r} \right) \Big|_{r=r_s^+} \Delta H_{vk} \\ &+ \dot{m} \left[ \frac{u^2}{2} - u \frac{dr_s}{dt} - \frac{1}{\rho} \left( 2\mu \frac{\partial u}{\partial r} + \frac{\lambda}{r^2} \frac{\partial}{\partial r} (ur^2) \right) \right] \end{aligned} \tag{9}$$

$$f_2(T_s, P_s, X_{1s}, X_{2s}, \dots, X_{Ns}, Y_{1s}, Y_{2s}, \dots, Y_{Ns}) = 0 \tag{10}$$

where  $\dot{m}$  is the droplet gasification rate, and  $X_{is}$  and  $Y_{is}$  represent, respectively, the liquid- and gas-phase mole fractions of  $i$ th species at the droplet surface. The specific form of Eq. (10) can be derived from the condition of thermodynamic and mechanical equilibrium at the droplet surface. At low pressures, the equilibrium is normally expressed by the Raoult’s law. However, at elevated pressures, it should be described from a more general thermodynamic consideration, as discussed in the Section 2.3.

The boundary conditions at the droplet center ( $r = 0$ ) are:  $\frac{\partial T_l}{\partial r} = 0$  and  $\frac{\partial \rho_{lk}}{\partial r} = 0$ , and those at  $r \rightarrow \infty$  are:  $T \rightarrow T_\infty, p \rightarrow p_\infty$ , and  $\rho_k \rightarrow \rho_{k\infty}$ .

In a supercritical environment, depending on the ambient and droplet properties, the droplet may experience a thermodynamic state transition from subcritical to supercritical. Eqs. (8)–(10) are only applicable until the droplet surface reaches a critical mixing point. At the critical mixing point, the droplet surface becomes indistinguishable from the gas phase. The subsequent droplet regression is then characterized by the motion of the critical surface which moves inward continuously.

### 2.3. Vapor–liquid equilibrium at the droplet surface

When the droplet surface is in mechanical and thermodynamic equilibrium, the temperature, pressure, and fugacity of each species in the gas phase is equal to the corresponding property of the same species in the liquid phase. The equality of fugacity of species  $k$  is expressed as:

$$\phi_k^v Y_k = \phi_k^l X_k \tag{11}$$

where the superscripts ‘v’ and ‘l’ refer to the vapor and liquid phase, respectively.  $\phi_k$  is the fugacity coefficient of  $k$ th species, and is a function of pressure, temperature, and composition. It is given in terms of the volumetric properties of the mixture by the following thermodynamic relation:

$$RT \ln(\phi_k) = \int_v^\infty \left[ \left( \frac{\partial P}{\partial n_k} \right)_{T, v, n_j} - \frac{RT}{v} \right] dv - RT \ln z \tag{12}$$

where  $z$  is the compressibility factor, and  $n_j$  is the mole number of  $j$ th species. By substituting the equation of state (5) into Eq. (12), the fugacity of the  $k$ th species in the liquid and gas phase mixture is given by [24]:

$$\ln \phi_k = \frac{b_k}{b}(z-1) - \ln(z-B) + \frac{A}{B\sqrt{u^2-4w}}$$

$$\left(\frac{b_k}{b} - \delta_k\right) \ln \left[ \frac{2Z + B(u + \sqrt{u^2 - 4w})}{2Z + B(u - \sqrt{u^2 - 4w})} \right] \quad (13)$$

where

$$\frac{b_k}{b} = \frac{T_{ck}/P_{ck}}{\sum_j y_j T_{cj}/P_{cj}} \quad \text{and}$$

$$\delta_k = \frac{2\sqrt{a_k}}{a} \sum x_j \sqrt{a_j} (1 - k_{kj})$$

The binary interaction coefficient  $k_{kj}$  in the above equation is taken from Knapp et al. [25]. It is 0.1441 for PR-EOS, and 0.1422 for SRK- and RK-EOS. Note that for a  $n$ -heptane–nitrogen system,  $k_{kj}$  for RK-EOS is not available in the literature. Consequently,  $k_{kj}$  for RK-EOS is assumed to be the same as that for SRK-EOS. This is based on the consideration that SRK-EOS is a modified version of RK-EOS. Eqs. (11)–(13) provide the basic relations for vapor–liquid equilibrium calculation. These equations along with Eqs. (8) and (9) provide a closed system to determine the temperature and species mole fractions at the droplet surface. It represents a system of highly nonlinear algebraic equations that need to be solved iteratively at each time step.

For a multicomponent mixture, the latent heat of vaporization of each species is defined as the difference between the partial molar enthalpy of that species in the vapor and liquid phases. The following thermodynamic relation then gives the partial molar enthalpy of  $k$ th species:

$$\bar{H}_k - \bar{H}_k^0 = -RT^2 \frac{\partial}{\partial T} (\ln \phi_k) \quad (14)$$

where the superscript ‘0’ denotes the quantity in an ideal state. Eq. (14) is solved iteratively along with Eqs. (8), (9) and (11)–(13).

#### 2.4. Thermophysical properties

The gas- and liquid-phase thermodynamic and transport properties are considered functions of pressure, temperature and composition. The method reported by Chung [26,27] is employed to calculate the thermal conductivity and viscosity of the gas mixture at high

pressures. The binary mass diffusivity is calculated by means of the Chapman–Enskog theory in conjunction with the collision integrals given in Ref. [28]. It is then corrected for pressure effects by using the Takahashi correlation [29]. For a multicomponent mixture, the effective diffusivity is obtained by using the formula given by Bird et al. [30]. The gas density is calculated directly from the EOS employed. For the enthalpy of gas mixture, the enthalpy of pure components is obtained from JANAF tables. A generalized thermodynamic correlation based on three-parameter corresponding states [31] is then used to calculate the enthalpy correction for high-pressure effects. Then, the specific internal energy of gas mixture in Eq. (3) is given by:

$$I = \sum_{k=1}^N \frac{\rho_k}{\rho} h_k(T) - \frac{p}{\rho} \quad (15)$$

which relates the energy Eq. (3) to the EOS (4) through the gas temperature.

The heat capacity of pure liquid components is calculated by a fourth-order polynomial of temperature, and is then extended to liquid mixture using the mixture rule of Filippov [32]. The liquid mass diffusivity and thermal conductivity are obtained by using the correlations of Nakanishi [33] and Chung [26], respectively. In the present study, two different methods are employed to determine the liquid density. In the first, the liquid density is obtained directly from the EOS employed, while in the second, it is calculated by using the formulae given in Ref. [34], along with the high-pressure correction given in Ref. [35].

#### 2.5. Numerical method

An arbitrary Lagrangian–Eulerian numerical method with a dynamically adaptive mesh is used to solve the above equations. The solution procedure is as follows:

1. calculate explicitly the contributions of the diffusion and source terms in the gas-phase equations;
2. calculate implicitly the terms associated with the acoustic pressure in the gas-phase equations;
3. compute new mesh distribution with the adaptive mesh method, and then the convection terms in the gas-phase equations; and
4. based on the solutions of above steps, solve implicitly the gas-phase equations, along with the liquid-phase equations as well as the droplet surface and vapor–liquid equilibrium equations.

In Step 3, the radial coordinate  $r_i$  of the adaptive mesh is calculated by:

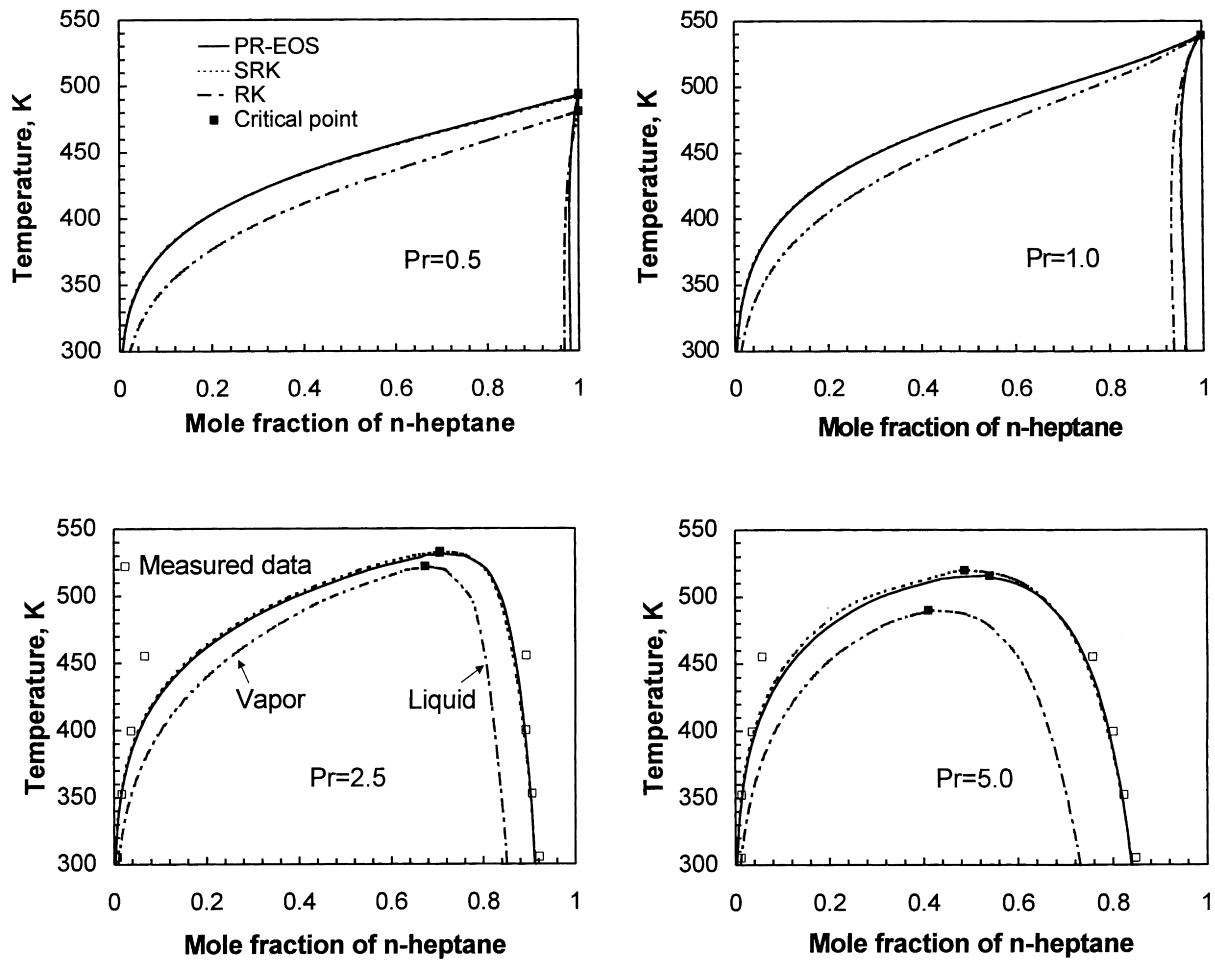


Fig. 1. Mole fraction of *n*-heptane predicted by PR-, SRK-, and RK-EOS for a *n*-heptane–nitrogen system in thermodynamic equilibrium at four different pressures.  $P_r$  is the reduced pressure normalized by the critical pressure of pure *n*-heptane. The experimental data from Ref. [26], for  $P_r = 2.5$  and  $5.0$ , are also included in the plots.

$$\int_{r_s}^{r_i} \left( \alpha_1 + \alpha_2 \frac{L}{\tau} \left| \frac{\partial T}{\partial r} \right| + \alpha_3 \frac{L^2}{\tau} \left| \frac{\partial^2 T}{\partial r^2} \right| \right) dr = \frac{i-1}{M}$$

$$\int_{r_s}^{r_\infty} \left( \alpha_1 + \alpha_2 \frac{L}{\tau} \left| \frac{\partial T}{\partial r} \right| + \alpha_3 \frac{L^2}{\tau} \left| \frac{\partial^2 T}{\partial r^2} \right| \right) dr \quad (16)$$

where  $\alpha_i$  are weighting factors that determine the mesh's relative sensitivity to the terms listed in the equation, and  $L$  and  $\tau$  are length and temperature scales used to non-dimensionalize the temperature derivatives. Further  $i$  is the mesh point index, and  $M$  the total mesh number. This adaptive mesh technique is very effective in improving the calculation efficiency and accuracy. For the supercritical vaporization calculations here, the results show that the minimum number of grid points for a uniform grid is about 600 in order to get a grid-independent solution. However,

using the adaptive mesh technique, the number of grid points is reduced to 180. A variable time-step is employed. It is calculated automatically based on the stability restrictions of explicit convection and diffusion processes.

### 3. Results and discussion

The present simulations consider a *n*-heptane droplet evaporating in a high-pressure nitrogen environment. The critical temperature and pressure of *n*-heptane are 540.2 K and 27.0 atm, respectively, while those of  $N_2$  are 126.2 K and 33.5 atm. First, results are presented that focus on the thermodynamic phase equilibrium obtained by using the PR-, SRK- and RK-EOS. Fig. 1 shows a comparison of the phase-equilibrium predic-

tions of PR-, SRK- and RK-EOS at four different pressures. An important observation is that PR- and SRK-EOS predict essentially the same equilibrium composition, including the fuel vapor mole fraction and the liquid-phase solubility of nitrogen, over a wide pressure range. There is a small difference in the prediction of the critical mixing state for these two EOS at  $P_r = 5.0$ . In contrast, the predictions of RK-EOS exhibit significant differences from those of PR- and SRK-EOS. In both the sub-critical and supercritical regimes, the RK-EOS predicts higher fuel vapor mole fraction, which implies that it would yield higher droplet gasification rate compared to that predicted by using the PR- and SRK-EOS. In addition, in the supercritical regime ( $P_r > 1.0$ ), the RK-EOS predicts higher mole fraction of liquid nitrogen or higher solubility of nitrogen in the liquid. This has important implications for the prediction of droplet gasification phenomena at supercritical pressures, as discussed later. The critical mixing point obtained by using RK-EOS is also markedly different from that obtained by using the other two EOS. The temperatures at the critical mixing point predicted by RK-EOS are 1.9 and 8.4% lower than those predicted by the other two EOS at  $P_r = 2.5$  and 5.0, respectively. In addition, the results for  $P_r = 2.5$  and 5.0 indicate that while the phase-equilibrium predictions of PR- and SRK-EOS show good agreement with the experimental data [25], those of RK-EOS show significant differences.

Another important observation from Fig. 1 pertains to the solubility of nitrogen into liquid at different ambient pressures and temperatures. At supercritical pressures, the amount of gas absorbed in the liquid phase becomes significant, and increases as the ambient temperature and pressure are increased. In addition, near the critical mixing point, both the vapor and liquid mole fractions of *n*-heptane exhibit strong sensitivity to the ambient temperature. Also notable in Fig. 1 is that the critical mixing temperature decreases as the pressure is increased. This is indicated more clearly in Fig. 2(a), which shows the pressure–temperature diagram for a *n*-heptane–nitrogen system in equilibrium. Again, the difference between the prediction of RK-EOS and those of SRK- and RK-EOS at supercritical pressures is significant.

Fig. 2(b) shows the variation of latent heat of vaporization of *n*-heptane with temperature as predicted by PR, SRK and RK-EOS at three different pressures. As expected, the heat of vaporization decreases as the temperature and/or pressure is increased, and drops to zero at the critical point. The predictions of PR- and SRK-EOS are again in good agreement with each other, while those of RK-EOS exhibit noticeable differences, with RK-EOS significantly underpredicting the heat of vaporization. As discussed later, this has important implications for the predictions of droplet

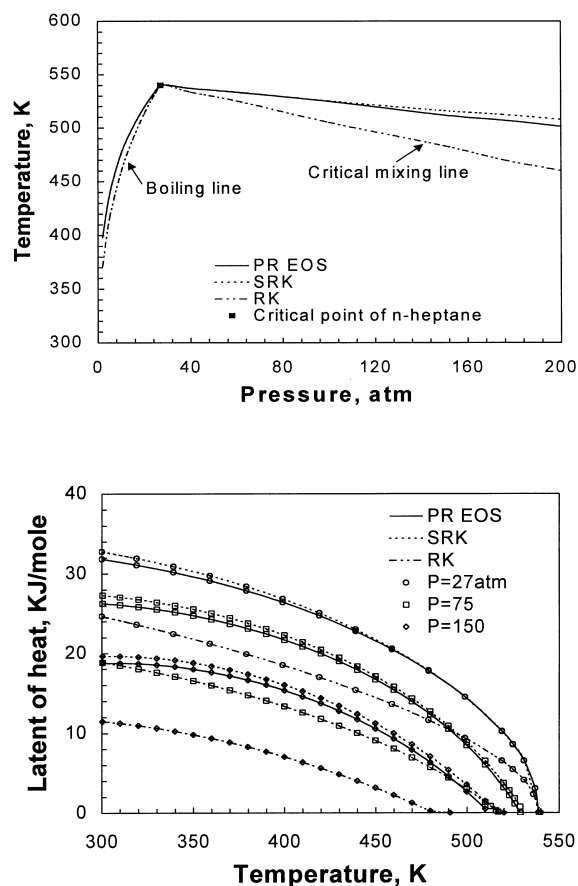


Fig. 2. (a) Phase equilibrium in terms of the pressure–temperature diagram, and (b) latent heat of vaporization of *n*-heptane versus temperature for *n*-heptane–nitrogen system in thermodynamic equilibrium, as predicted by PR-, SRK-, and RK-EOS at three different pressures. See Fig. 1 for additional details.

vaporization rate at supercritical conditions using different EOS.

The following results focus on the transient vaporization of a *n*-heptane droplet which at time  $t = 0$  is introduced into a high-pressure nitrogen environment. The droplet initially is at sub-critical state with a temperature of 300 K and diameter of 0.5 mm. In order to evaluate the real gas effects, the compressibility factor predicted by using PR-, SRK-, and RK-EOS is plotted as a function of radial location in the gas-phase region, see Fig. 3. Results are shown for three different pressures. As expected, deviation of the compressibility factor from unity becomes more noticeable at high ambient pressures. However, its variation is confined to a narrow region which is of the order of droplet radius (dimensionless radius less than 5.0). The maximum departure from unity occurs at the first finite-

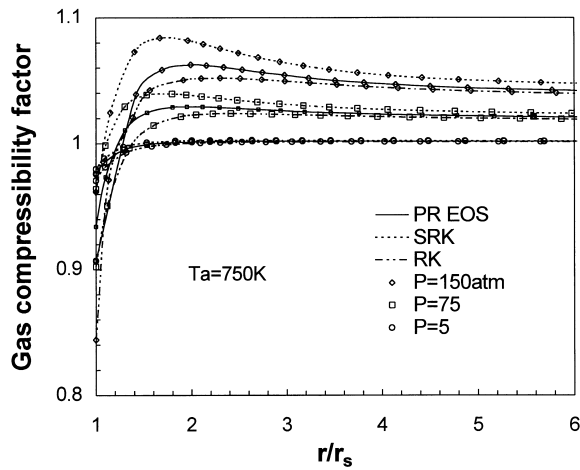


Fig. 3. Gas compressibility factor plotted as a function of radial location in the gas-phase region, as predicted by using PR-, SRK-, and RK-EOS at three different pressures. Results are plotted at a time when the non-dimensional droplet surface area is 0.5.

difference node from the droplet surface, where the fuel vapor mass fraction and gas temperature have the maximum and the minimum value, respectively.

Fig. 4 shows the droplet lifetime computed by using different EOS and plotted as a function of pressure for three different ambient temperatures. Here, the droplet lifetime is defined when the non-dimensional droplet surface area reaches a value of 0.2, and normalized by using a characteristic time as  $d_0^2/\beta$ , where  $d_0$  is the initial diameter, and  $\beta$  is the vaporization constant com-

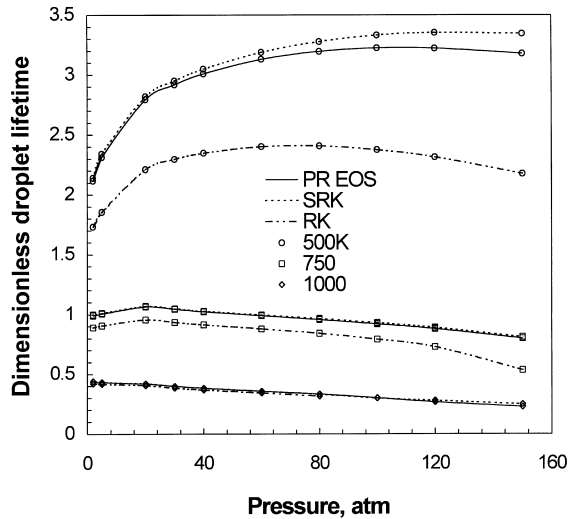


Fig. 4. Non-dimensional droplet lifetime, predicted by PR-, SRK-, and RK-EOS, plotted versus pressure at three different ambient temperatures.

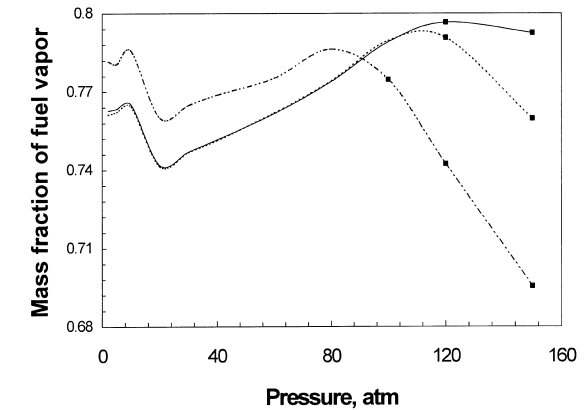
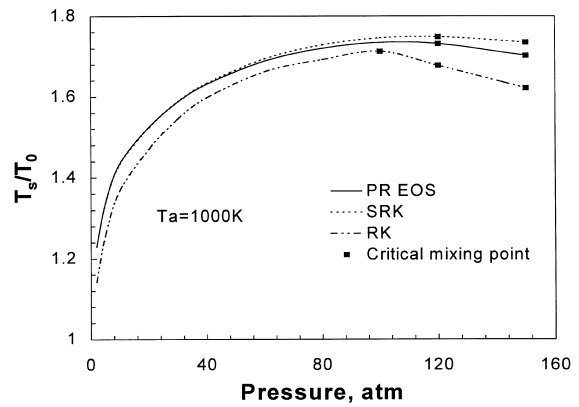


Fig. 5. Final temperature and fuel vapor mass fraction at the droplet surface plotted as functions of pressure. The ambient temperature ( $T_a$ ) is 1000 K, and initial droplet temperature ( $T_0$ ) 300 K. The final time corresponds to a time when  $(d/d_0)^2 = 0.2$ .

puted at  $p = 1\text{atm}$  and  $T_a = 750\text{K}$ . At high ambient temperatures, the droplet lifetime decreases monotonically as the ambient pressure is increased. However, at low to moderate ambient temperatures, the droplet lifetime first increases and then decreases as the ambient pressure is increased. This behavior, which is in accord with the published experimental results [21], can be explained as follows.

As ambient pressure increases, it causes following effects:

1. the droplet heatup time increases and becomes a more significant part of the droplet lifetime, since the fuel boiling temperature increases with pressure until the droplet surface reaches a critical state, see Fig. 2(a);
2. the mass transfer number  $B$ , which is generally expressed as  $B = C_p(T_a - T_s)/L$ , decreases since  $T_s$  increases with pressure;
3. the latent heat of vaporization ( $L$ ) decreases and

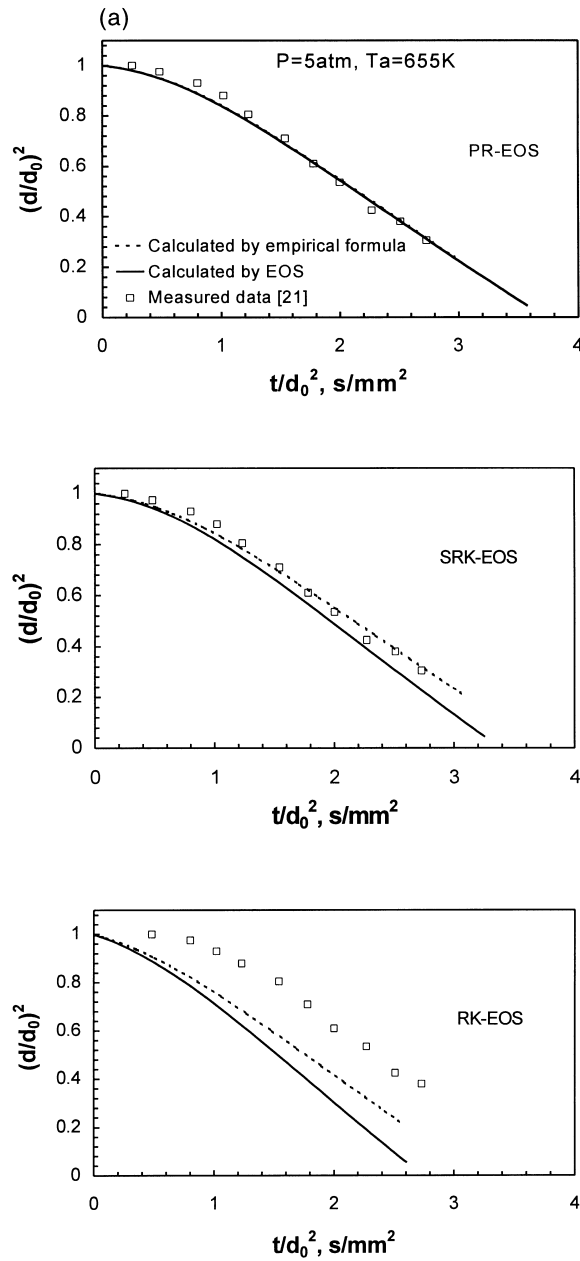


Fig. 6. Comparison between the predictions of PR-, SRK-, and RK-EOS and the measured data from Ref. [21] at two different ambient conditions.

drops to zero as the droplet surface reaches a critical mixing point, see Fig. 2(b).

At low to moderate ambient temperatures, the first two effects dominate. Consequently, the droplet lifetime increases with pressure. However, at higher pressures, the third effect becomes more dominant, since the heat of vaporization decreases drastically and goes to zero at the critical mixing point. Consequently, as indi-

cated in Fig. 4 for ambient temperatures of 500 and 750 K, the droplet lifetime decreases with pressure at high pressures. Also, when the ambient temperature is sufficiently high, the first two effects become relatively less sensitive to pressure compared with the third effect, and the droplet lifetime decreases continuously as the ambient pressure is increased. These results also imply that the lifetime of a combusting droplet would

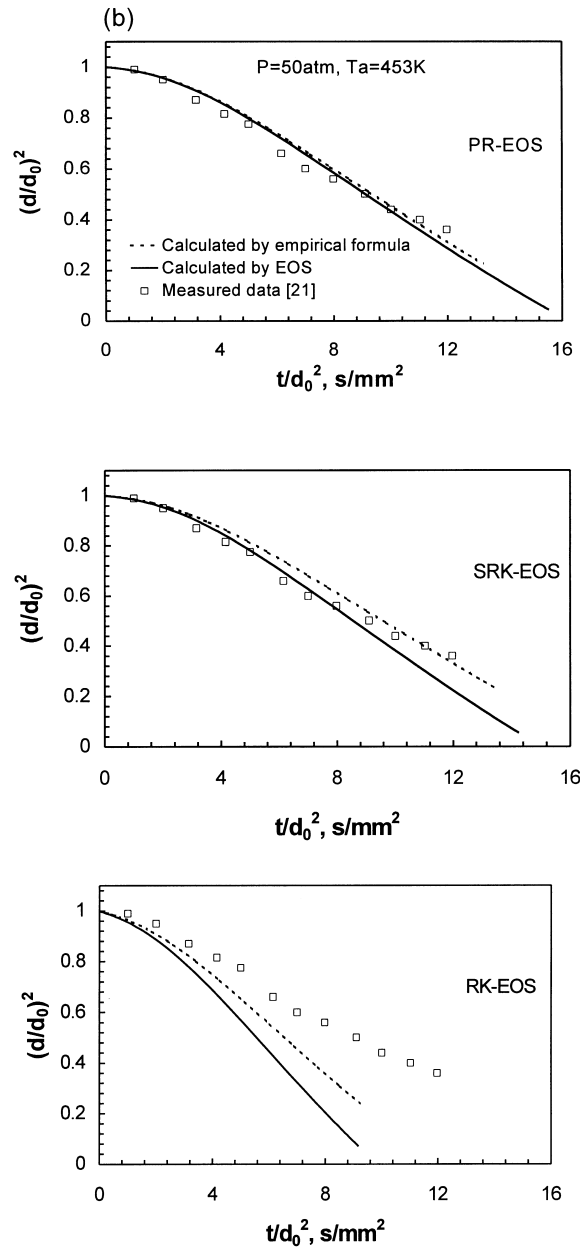


Fig. 6 (continued)

decrease monotonically with increasing ambient pressure. This observation is well corroborated by several experimental studies [21,36]. Jia and Gogos [15] have reported similar results for an evaporating *n*-hexane droplet.

The sensitivity of the computed droplet lifetime to the three EOS is also illustrated in Fig. 4. For all the cases examined, the lifetime predictions using PR-EOS

and SRK-EOS are in good agreement with each other, except for small differences at low ambient temperatures ( $T = 500\text{ K}$ ) and at high pressures ( $p > 60\text{ atm}$ ). In contrast, at moderate ambient temperatures ( $T_a = 750\text{ K}$ ), RK-EOS significantly underpredicts the droplet lifetime compared with those obtained by using PR- and SRK-EOS. This can be attributed to the fact that for given ambient temperature and press-

ure, RK-EOS predicts higher fuel vapor mole fraction at the droplet surface and lower heat of vaporization compared with those predicted by PR- and SRK-EOS, see Figs. 1 and 2(b). At high ambient temperatures, however, the differences in the lifetime predictions using the three EOS are insignificant. This implies that the predicted gasification behavior of a combusting droplet may not be sensitive to the particular EOS used.

In Fig. 5, we plot the final temperature and fuel vapor mass fraction at the droplet surface versus the ambient pressure. Again, the predictions of SRK- and PR-EOS are in close agreement over a wide pressure range, except for small deviations after the droplet surface reaches the critical mixing state. The predicted droplet surface temperature using RK-EOS is slightly lower than that predicted by using the other two EOS. More importantly, the predicted fuel vapor mass fraction using RK-EOS is higher compared to those obtained by using SRK- and PR-EOS prior to the attainment of critical state, and lower after the critical state is reached. This is consistent with the phase-equilibrium results presented in Fig. 1, which indicates higher fuel vapor mass fraction for RK-EOS. The results for  $P_r = 5.0$  in Fig. 1 also indicate that RK-EOS leads to the attainment of a critical mixing point at a lower temperature compared to that for the other two EOS. After the critical state is reached, the final temperature and fuel vapor mass fraction at the droplet surface decrease as the pressure is increased. This behavior is consistent with the phase-equilibrium results in shown Fig. 2(a), which indicates that the critical temperature decreases with critical pressure, as well as with those reported in Ref. [12,15].

As noted earlier, the literature indicates a wide scatter in the minimum ambient pressure required for attaining a critical mixing state at the droplet surface. Clearly, a reliable supercritical droplet gasification model should provide an accurate value of this pressure. As indicated in Fig. 5, at an ambient temperature of 1000 K, the minimum ambient pressure predicted by using PR- and SRK-EOS is 120 atm ( $P_r = 4.44$ ), while that by using RK-EOS is 100 atm ( $P_r = 3.70$ ).

In Fig. 6, we compare our predictions with experimental data taken from Ref. [21]. Results are presented in terms of the temporal variation of non-dimensional surface area obtained by using the three EOS for two different ambient conditions. In order to examine the effect of liquid density on predictions, the computed results are shown for two cases. In the first case, the liquid density is calculated directly from the respective EOS, while in the second case, it is calculated from an empirical formula [34,35]. An important observation is that using PR-EOS, the simulations reproduce experimental results quite well over a wide range of pressures. The numerical results obtained by

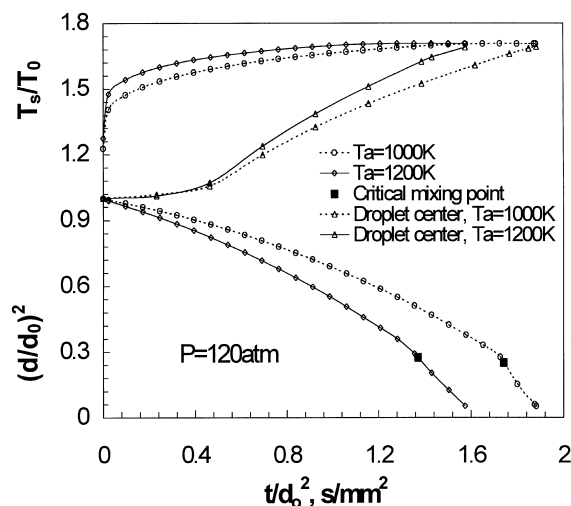


Fig. 7. Supercritical vaporization behavior in terms of the temporal variation of non-dimensional droplet surface area, surface temperature and liquid temperature at the droplet center, as predicted by PR-EOS. The ambient pressure is  $P = 120$  atm.

using SRK-EOS are also in good agreement with experimental data, while those obtained by using RK-EOS exhibit significant differences, especially for the high-pressure case. Consistent with the earlier discussion, the RK-EOS significantly overpredicts the vaporization rate and, thus, underpredicts the droplet lifetime. For example, for  $p = 50$  atm and at a non-dimensional time of 8, the numerical model based on RK-EOS predicts a non-dimensional surface area of 0.2 compared to the experimental value of 0.6. The predictions of RK-EOS show noticeable improvement when the liquid density is calculated by the empirical formula, but still deviate from the experimental data.

In order to further examine the supercritical droplet vaporization phenomena, we now present the variation of some important gas- and liquid-phase properties during the transcritical state. Fig. 7 shows the temporal variation of droplet surface area, surface temperature and liquid temperature at the droplet center for an ambient pressure of 120 atm. The predictions are based on PR-EOS with liquid density calculated by using the empirical formula. As indicated, the droplet surface, which is initially at a subcritical state, reaches the critical mixing state during a later part of droplet lifetime. Higher the ambient temperature is, more rapidly does the surface temperature rise, and earlier in lifetime does the surface reach the critical mixing state.

Although some experimental studies [21] have observed anomalies in the transport properties near the critical point, no such behavior was observed in the present study. Curtis and Farrell [8] reported that

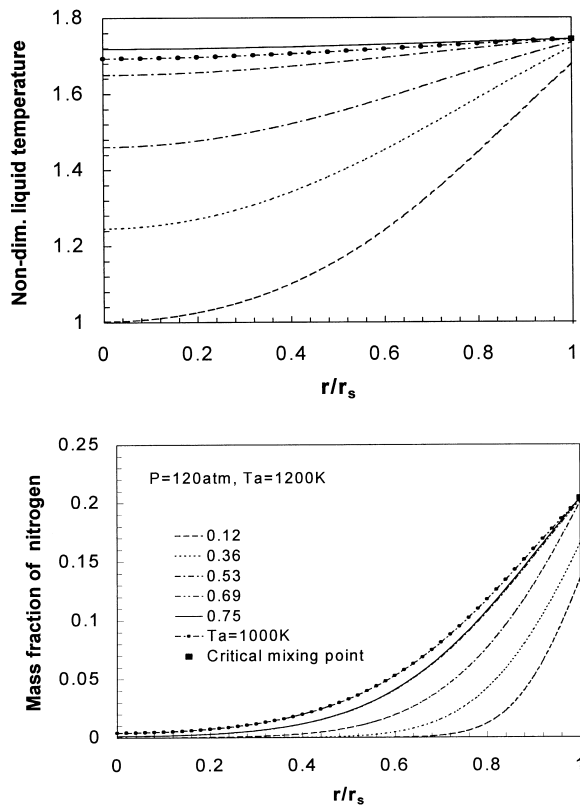


Fig. 8. Radial distribution of liquid temperature (a) and dissolved nitrogen (b) in the droplet interior at different times, as predicted by PR-EOS.

these anomalies had negligible influence on droplet vaporization. When the droplet surface approaches the critical mixing state, the difference between the gas and liquid phases disappears. In the present model, it is assumed that once the surface reaches the critical mixing state, it is maintained at that state.<sup>2</sup> The velocity of the critical mixing surface moving inwards to the droplet center then determines the vaporization rate. This velocity depends on how fast the inner liquid layer adjacent to the droplet attains the critical mixing temperature, which in turn depends on the distributions of liquid-phase properties within the droplet.

Fig. 8 shows the radial distribution of liquid temperature and dissolved nitrogen within the droplet during different stages of droplet lifetime. The ambient conditions are the same as those in Fig. 7. As expected, the liquid nitrogen mass fraction has its maximum value at the droplet surface, and increases continuously with time until the droplet surface

<sup>2</sup> Note, however, that the critical mixing state varies with ambient temperature and pressure.

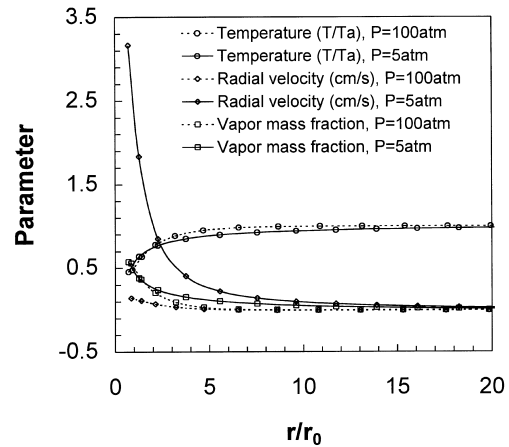


Fig. 9. Radial distribution of gas temperature, velocity, and fuel vapor mass fraction in the gas-phase region as predicted by PR-EOS for two ambient pressures of 5 and 150 atm.

reaches a critical mixing state. Note that the critical mixing state for this case is attained at a non-dimensional time of 0.69. This plot clearly demonstrates that a pure fuel droplet evaporating in a supercritical environment exhibits multicomponent behavior. It is also noteworthy that while the liquid nitrogen mass fraction drops rapidly to a negligible value within a thin layer near the surface, the liquid temperature shows a more gradual decrease. This is indicative of small liquid mass diffusivity (relative to thermal diffusivity) or high liquid Lewis number.

Fig. 9 shows the radial distribution of gas temperature, velocity, and fuel vapor mass fraction in the gas-phase region at two different ambient pressures. For

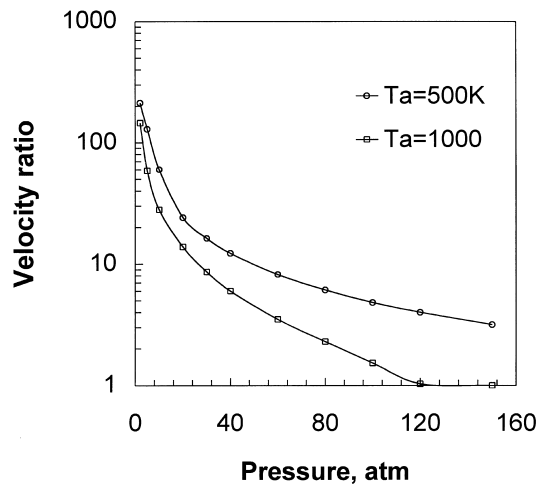


Fig. 10. Ratio of the maximum gas velocity to the rate of change of droplet diameter plotted versus ambient pressure for two different ambient temperatures.

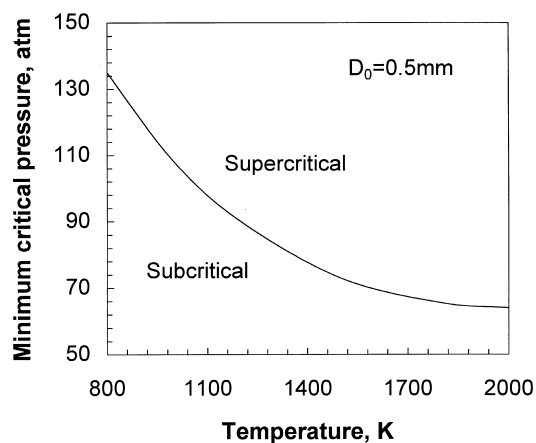


Fig. 11. Minimum pressure, required for a *n*-heptane fuel droplet to attain a critical mixing state, plotted as a function of ambient temperature. The initial diameter is 0.5 mm. The critical temperature and pressure of *n*-heptane are 540.2 K and 27.0 atm, respectively.

these results, the PR-EOS has been employed. An important observation is that the radial distance over which the gas-phase properties vary significantly decreases as the ambient pressure is increased. For example, it decreases from ten to four times the droplet radius as the pressure is increased from 5 to 150 atm. This implies that the rates of heat and mass transport are enhanced, and, consequently, the vaporization rate is increased at higher pressures. It can be seen that the maximum gas velocity decreases dramatically when the pressure is increased from 5 to 150 atm, which implies a change in the gas-phase unsteadiness. The simulations also indicated that the pressure variation in the gas-phase was negligible. For example, at 100 atm and 750 K the maximum pressure difference, normalized by the ambient pressure, was of order  $O(10^{-4})$ .

In Fig. 10, we plot the ratio of the maximum gas velocity to the rate of change of droplet diameter as a function of pressure for different ambient temperatures. At low to moderate pressures, the velocity ratio decreases rapidly as the pressure is increased. For example, at an ambient temperature of 1000 K, this ratio decreases from about 100 to 10 as the pressure is increased from about 5 to 25 atm. This implies a significant increase in the gas-phase unsteadiness with the ambient pressure. Therefore, even at moderate pressures, the gas-phase unsteadiness may be important. Also note that when the droplet surface reaches the critical mixing state, the velocity ratio becomes unity; which represents an extreme in gas-phase unsteadiness. For the results shown in Fig. 10, the critical mixing state is achieved for the ambient temperature of 1000 K.

As mentioned earlier, the literature indicates a wide scatter in the minimum ambient pressure required for a droplet to attain a critical mixing state at its surface. Clearly, this value depends on various liquid- and gas-phase properties including ambient temperature and composition, initial droplet diameter, and liquid fuel properties. Fig. 11 shows this minimum ambient pressure as a function of ambient temperature. In order to obtain a minimum pressure value at fixed ambient temperature, simulations were performed for increasingly higher pressures until a critical mixing state is observed at the droplet surface. The plot in Fig. 11 represents a boundary, in terms of the ambient temperature and pressure, between the subcritical and supercritical vaporization. Any point above the curve indicates that a critical mixing state will be reached sometime during the droplet lifetime, i.e., the droplet will undergo transcritical evaporation during its lifetime. On the other hand, any point below the curve implies that the droplet is not expected to attain a supercritical state during its lifetime. Also, farther a point is from the curve in the supercritical region, earlier in its lifetime is the droplet expected to attain a critical mixing state.

#### 4. Conclusions

In this paper, a comprehensive investigation of the transcritical droplet vaporization phenomena has been conducted. The physical–numerical model considers the transient, spherically-symmetric conservation equations for both gas and liquid phases, pressure-dependent variable thermophysical properties, and a detailed treatment of the liquid–vapor phase equilibrium at the droplet surface. The model is shown to reproduce the subcritical, transcritical, and supercritical vaporization behavior of a liquid fuel droplet over a wide range of ambient conditions. In addition, the effects of using three different EOS on predicting the equilibrium composition and transcritical droplet vaporization have been examined. Important observations are as follows:

1. The phase-equilibrium results for an *n*-heptane–nitrogen system using RK-EOS show significant differences from those using PR- and SRK-EOS, as well as from the experimental data. The RK-EOS yields higher fuel vapor concentration, higher solubility of nitrogen into liquid, lower critical-mixing-state temperature, and lower latent heat of vaporization compared to those obtained by using PR- and SRK-EOS. In contrast, the phase-equilibrium predictions of PR- and SRK-EOS are in good agreement with the experimental data.
2. At low to moderate ambient temperatures, RK-EOS significantly overpredicts the droplet vaporization rate and, thus, underpredicts the droplet lifetime

compared to that predicted by using the other two EOS. This is essentially attributable to differences in the phase-equilibrium predictions of the three EOS. Furthermore, using RK-EOS, attainment of the critical mixing state at the droplet surface is predicted earlier in droplet lifetime compared to that by using the other two EOS. These differences become less noticeable at higher ambient temperatures ( $T_a \geq 1000$  K), implying that differences between the predictions of three EOS for combust- ing droplets may not be significant.

3. The droplet lifetime predictions using PR-EOS are in excellent agreement with the reported measurements [21] over a wide range of ambient pressures. In contrast, the predicted results based on RK-EOS show significant differences with measurements, while those based on SRK-EOS are in reasonably good agreement with measurements.
4. At low to moderate ambient temperatures, the predicted droplet lifetime first increases reaching a maximum value, and then decreases as the ambient pressure is increased. At high ambient temperatures ( $T_a \geq 1000$  K), however, the droplet lifetime decreases monotonically with increasing pressure. These results are in accord with the reported exper- imental and numerical results [19–21].
5. As noted earlier, the literature indicates wide scatter in the value of the minimum pressure required for attaining critical-mixing state at the droplet surface. In the present study, the numerical model is used to obtain this minimum pressure as a function of ambi- ent temperature. The plot of this function represents a boundary between the subcritical and supercritical droplet vaporization.

### Acknowledgements

This work was partially funded by the GE Aircraft Engines.

### References

- [1] J.A. Manrique, G.L. Borman, Calculation of steady state droplet vaporization at high ambient pressures, *Int. J. Heat Mass Transfer* 12 (1969) 1081–1095.
- [2] P.L. Chueh, J.M. Prausnitz, Calculation of high pressure vapor–liquid equilibria, *Ind. Engng Chem* 60 (1968) 34–52.
- [3] C.W. Savery, G.L. Borman, Experiments on droplet vaporization at supercritical pressures, *AIAA Paper No. 70-6*, 1970.
- [4] R.S. Lazar, G.M. Faeth, Bipropellant droplet combustion in the vicinity of the critical point, in: *Proceedings Thirteenth Symposium (International) on Combustion*, 1971, pp. 801–811.
- [5] G.S. Canada, G.M. Faeth, Fuel droplet burning rates at high pressures, in: *Proceedings of Fourteenth Symposium (International) on Combustion*, 1973, pp. 1345–1354.
- [6] R.L. Matlosz, S. Leipziger, T.P. Torda, Investigation of liquid drop evaporation in a high temperature and high pressure environment, *Int. J. Heat Mass Transfer* 15 (1972) 831–852.
- [7] E.W. Curtis, P.V. Farrell, Droplet vaporization in a supercritical microgravity environment, *Acta Astronautica* 17 (1988) 1189–1193.
- [8] E.W. Curtis, P.V. Farrell, A numerical study of high-pressure droplet vaporization, *Combust. Flame* 90 (1992) 85–102.
- [9] D. Peng, D.B. Robinson, A new two-constant equation of state, *Indust. Eng. Chem. Fund* 15 (1976) 59–64.
- [10] K.C. Hsieh, J.S. Shuen, V. Yang, Droplet vaporization in high pressure environments. Part I: Near critical conditions, *Combust. Sci. and Tech* 76 (1991) 111–132.
- [11] M.S. Graboski, T.E. Daubert, A modified Soave equation of state for phase equilibrium calculations. Part I: Hydrocarbon systems, *Industrial and Engineering Chemistry Process Design and Development* 17 (1987) 337–443.
- [12] J.S. Shuen, V. Yang, C.C. Hsiao, Combustion of liquid-fuel droplets in supercritical conditions, *Combust. Flame* 89 (1992) 299–319.
- [13] J.P. Delplanque, W.A. Sirignano, Numerical study of the transient vaporization of an oxygen droplet at sub- and super-critical conditions, *Int. J. Heat Mass Transfer* 36 (1993) 303–314.
- [14] H. Jia, G. Gogos, Investigation of liquid droplet evaporation in subcritical and supercritical gaseous environments, *J. of Thermophysics and Heat Transfer* 6 (1992) 738–745.
- [15] H. Jia, G. Gogos, High pressure droplet vaporization; effects of liquid-phase gas solubility, *Int. J. Heat Mass Transfer* 36 (1993) 4419–4431.
- [16] J. Stengele, H.J. Bauer, S. Wittig, Numerical study of bicomponent droplet vaporization in a high pressure environment, in: *Presented at the International Gas Turbine and Aeroengine Congress and Exhibition*, Birmingham, UK, Paper No. 96-GT-442, 1996.
- [17] S.K. Aggarwal, Z. Shu, H. Mongia, H.S. Hura, Multicomponent and single-component fuel droplet evaporation under high pressure conditions, *AIAA Paper No. 98-3833*, 1998.
- [18] R. Ruszalo, W.L.H. Hallett, A model for the autoignition of single liquid droplets at high pressure, *Combust. Sci. and Tech* 86 (1992) 183–197.
- [19] S.D. Givler, J. Abraham, Supercritical droplet vaporization and combustion studies, *Prog. Energy Combust. Sci* 22 (1996) 1–28.
- [20] H. Kawazoe, K. Ohsawa, K. Fujikake, LDA measurement of fuel droplet sizes and velocities in a combustion field, *Combust. Flame* 82 (1990) 151–162.
- [21] H. Nomura, Y. Ujiie, H.J. Rath, J. Sato, M. Kono, Experimental study of high-pressure droplet evaporation using microgravity conditions, in: *Twenty-Sixth*

- Symposium (International) on Combustion, The Combustion Institute, 1996, pp. 1267–1273.
- [22] G.M. Faeth, Current status of droplet and liquid combustion, *Prog. Energy Combust. Sci* 3 (1977) 191–224.
- [23] C. Tsonopoulos, J.L. Heidman, From Redlich–Kwong to the present, *Fluid Phase Equilibria* 24 (1985) 1–23.
- [24] R.C. Reid, J.M. Prausnitz, B.E. Poling, *The Properties of Gases and Liquids*, McGraw-Hill, New York, 1987.
- [25] H. Knapp, R. Doring, L. Oellrich, U. Plocker, J.M. Prausnitz, Vapor–liquid equilibria for mixture of low boiling substances, in: *Chemical Engineering Data Series*, vol. VI, DECHEMA, Frankfurt, 1982.
- [26] T.H. Chung, M. Ajlan, L.L. Lee, K.E. Starling, Generalized multiparameter correlation for nonpolar and polar fluid transport properties, *Ind. Engng Chem. Res* 27 (1988) 671–679.
- [27] T.H. Chung, L.L. Lee, K.E. Starling, Applications of kinetic gas theories and multiparameter correlation for prediction of dilute gas viscosity and thermal conductivity, *Ind. Engng Chem. Fundam* 23 (1984) 8–13.
- [28] P.D. Neufeld, A.R. Janzen, R.A. Aziz, Empirical equations to calculate 16 of the transport collision integrals  $\Omega^{(l,s)}$  for the Lennard–Jones potential, *J. Chem. Phys* 57 (1972) 1100–1102.
- [29] S. Takahashi, Preparation of a generalized chart for the diffusion coefficients of gases at high pressures, *J. Chem. Engng. Japan* 6 (1974) 417–420.
- [30] R.B. Bird, W.E. Stewart, E.N. Lightfoot, *Transport Phenomena*, Wiley, New York, NY, 1960.
- [31] I.L. Byung, G.K. Michael, A generalized thermodynamic correlation based on three-parameter corresponding states, *J. AIChE* 21 (1975) 510–527.
- [32] L.P. Filippov, Thermal conduction of solutions in associated liquids: thermal conduction of 50 organic liquids, *Chem. Abstr.* 49 (1955) 15430–15431 and 50 (1956) 8276.
- [33] K. Nakanishi, Prediction of diffusion coefficients of nonelectrolytes in dilute solution based on generalized Hammond–Stokes plot, *Ind. Engng. Chem. Fundam* 17 (1978) 253–256.
- [34] R.W. Hankinson, G.H. Thomson, A new correlation for saturated densities of liquids and their mixtures, *J. AIChE* 25 (1979) 653–663.
- [35] G.H. Thomson, K.R. Brobst, R.W. Hankinson, An improved correlation for densities of compressed liquids and liquid mixtures, *J. AIChE* 28 (1982) 671–676.
- [36] K. Kadota, H. Hiroyasu, Combustion of a fuel droplet in supercritical gaseous environments, in: *Eighteenth Symposium (International) on Combustion*, The Combustion Institute, 1982, pp. 275–282.